Numerical study of icebreaking process with two different bow shapes based on developed particle method in parallel scheme

Yuan Zhang [a], Longbin Tao [b], Chao Wang [a, *], Liyu Ye [a**], Shuai Sun [c]

[a] College of Shipbuilding Engineering, Harbin Engineering University, Harbin 150001, China

[b] Department of Naval Architecture and Marine Engineering, University of Strathclyde, Glasgow G4 0LZ, United Kingdom

[c] National Key Laboratory of Transient Physics, Nanjing University of Science and Technology, Nanjing 210094, China

ABSTRACT

The bow shape is the most critical factor to determine the icebreaking performance of an icebreaker. Mechanism study on the icebreaking process for different bow types is necessary for the initial design of the icebreaker hull form. This paper proposed an ice-ship interaction model based on the meshfree method, Peridynamics, in which the geometric mathematics concept is embedded to detect the contact between material points and ship hull. Furthermore, a fast contact detection algorithm based on Massage Passing Interface (MPI) solver is built to improve the computational efficiency of the developed numerical method. Two typical icebreaker bows, the conventional bow and the unconventional bow, breaking the level ice with constant speed is numerically studied by the above model. The results of the conventional icebreaker bow are compared with the experimental results, which verifies the simulation accuracy of the model developed in the present work. Afterwards, the icebreaking modes and icebreaking loads of two different shapes of icebreaker bows are compared and analysed. The results show that the developed ice-ship interaction model effectively predicts differences of icebreaking processes between different icebreakers, such as ice damage pattern, ice loads, and channel, despite their common point in domain bending failure mode. Moreover, this research significantly improves computational efficiency and provides theoretical guidance for designing the icebreaker bow.

Key Words： Ice-ship interaction model, Fast contact detection algorithm, Peridynamics, Icebreaker bow shapes;

1. Introduction

With increased shipping activities, scientific investigation, resource exploitation, and military application value in arctic regions, the demand for high-performance ice-going ships rises accordingly (Gao and Erokhin, 2020; Larsen et al., 2016; Skripnuk et al., 2020). The icebreaker is a special-purpose ship designed to move and navigate through ice-covered waters and provides safe waterways for other ice-going ships. The bow is the main component to break the ice layer and push ice pieces, so the bow shape largely determines the icebreaking efficiency, icebreaking mode, and ice movement trajectory. Icebreaker bow also directly affects the clearing efficiencies by submerging broken ice in different ways (Guard, 1972; Riska, 2011). Consequently, understanding the influence of bow profile characteristics on the icebreaking process contributes to the design consideration and performance evaluation of icebreakers and helps guide the ice navigation in addressing the ice condition for different icebreakers. This makes it necessary numerically investigate and analyse the icebreaking mode of different bow shapes.

Five characteristic parameters describe the shape of icebreakers bow: flare angle, waterline angle, buttock angle, stem angle, and bow length (Aamot, 2015; Dick and Laframboise, 1989; Hu and Zhou, 2015; Sodhi, 1995). The ship's ability to break the ice layer and submerge floating broken ice floes is mainly determined by the flare angle, while the removal of brash ice accumulated on both sides and in front of the bow largely depends on the waterline angle. The buttock angle and stem angle are the secondary parameters that influence the icebreaking process and sinking of the broken ice. Therefore, the bow design revolves around the characteristics mentioned above according to ice conditions and icebreakers' mission planning. According to the outline, the typical icebreaker bow can be divided into conventional bows and unconventional bows. The conventional bows, including straight bow with parallel buttocks, concave bow (White bow), high flare angle bow (Melville bow), have smooth hulls and good resistance performance in open water. The unconventional bow shapes are further classified as spoon-shaped bow with reamers, half spoon-shaped bow with chines, flat bow, and Thyssen-Waas bow (Jones, 2008; Jones, 2004;

Sodhi, 1995). In this paper, a conventional straight bow with parallel buttocks and an unconventional Thyssen-Waas bow are modeled to investigate the differences in the icebreaking process.

The research on the icebreaking process of different bow shapes started as early as the 18th century; at the very beginning of the icebreaker appearance, there were few special regulations or recommendations on the icebreaker bow design except a larger machinery power in icebreakers. Not until the 19th century, icebreaker design developed much with several technological innovations; a very small stem angle β characterised the bow shape in this time, and the rounded stem that emerged as a sharp bow in the 1980s had always been considered to be desirable for icebreaking (Riska, 2019). White (1969) predicted the performance of the icebreaking bow using a purely analytical method and summarised its' characteristics, which would be beneficial for improving icebreaking capability. Proc. 6th STAR Symposium compared and analysed resistance performance of icebreaker with different bow shapes according to the model tests carried out by different organisations. The results showed that the rounded bows with low stem angle performed best in breaking ice (Michailidis and Murdey, 1981; Noble and Bulat, 1981; Schwarz et al., 1981). In the 1990s, the INSROP, International Northern Sea Route Programme, carried out a series of model tests for icebreakers' design and summarised the effect of ship bow shape on icebreaking resistance in low and high ship speed range. It is concluded that the smaller the stem angle, the lower the icebreaking resistance (Ishikawa and Kawasaki, 1995; Izumiyama and Uto, 1995; Kishi and Narita, 1995; Suzuki et al., 1997; Yamaguchi et al., 1997). Ierusalimsky and Tsoy (1994) and Glen et al. (1998) carried out a series of comparison model tests on different bow forms and concluded that the non-traditional bows showed better icebreaking performance in level ice but poorer performance in open water. Warntjen et al. (2018) studied the relationship between the structural response and the bow shape by MATLAB and revealed that the smaller buttock angle and the average waterline angle are conducive to reduce ice resistance in the channel. Tao et al. (2019) developed a prototype parametric icebreaker model using CAESES software and established the qualitative relationship between the main factor of bow shape and the ice resistance. The icebreaking force, mainly dependent on the bow shape, contributes a lot to the icebreakers' resistance to level ice (Puntigliano, 2003; Riska, 2011; Valanto, 2001).

Moreover, some theoretical methods, including empirical or semi-empirical formulas, have been proposed and applied to predict icebreaking force (Lindqvist, 1989; Lindstrom, 1990; Sawamura, 2012; Su et al., 2010); for example, the influence of icebreaking patterns and geometric bow parameters on icebreaking resistance was researched and evaluated by model tests (Myland and Ehlers, 2016). It is found that the research on the differences in the icebreaking process among different bow shapes mainly relies on the conclusions from early experiments and analysis. There is still a lack of efficient or accurate numerical methods for the comparative study of the detailed phenomenon and mechanism of the icebreaking process.

As for the numerical study on the ice-ship interaction, much work has been done to capture the further physical process of ice-ship interaction, which was reviewed in a very recent article (Xue et al., 2020). Of all the methods reviewed in Xue et al. (2020), the meshfree particle methods, such as Smoothed Particle Hydrodynamics (SPH) and Peridynamics (PD), demonstrated their superior and robust potential to solve ice damage problems. The PD method especially predicts the evolution of crack propagation in ice failure realistically and accurately with its own fracture criterion. This was well demonstrated by previous work: ice-propeller interaction (Wang et al., 2018; Ye et al., 2017), submarine surfacing through ice (Ye et al., 2020), and ice-structure interaction (Vazic et al., 2019). Therefore, the meshfree particle method, PD, is utilised as the basic methodology for the ice model in the present paper.

The present work aims to analyse the differences in icebreaking modes and icebreaking loads between a traditional and a non-traditional bow using numerical simulation. For this purpose, a meshfree method-based ice-ship interaction (ISI) model, which embedded a proposed fast contact detection algorithm into PD theory, is developed to achieve the numerical model. This is introduced in Section 2 and Section 3. Furthermore, in Section 4, the MPI parallel scheme is developed to the framework of the above numerical model to improve computational efficiency. The numerical prediction program is compiled in the FORTRAN language environment, and the specific programming strategy is presented in Section 5. Finally, the icebreaking process of two typical bow shapes is predicted in Section 6. The comparison between numerical results with conventional bow and experiment data shows reasonable and efficient prediction, verifying the present model. Then, the differences in icebreaking mode and icebreaking loads of two kinds of icebreaker bow are concluded and analysed.

The unique contributions of the present paper are summarised here:

1) A fast contact detection algorithm (FCDA) for ISI is proposed to solve the impact between the material particle calculation domain and the solid body. The FCDA can be applied to various numerical engineering applications that relate to the collision of irregular-shaped objects. The numerical strategy for FCDA is demonstrated here, in Section 5.1.
2) The MPI parallelisation for the PD theory, one of the frameworks of the meshfree particle method, is first introduced to the developed ISI model, and the numerical analysis for ISI in MPI scheme is conducted in Section 5.3.
3) The above-developed method is applied to engineering cases, icebreaker breaking level ice, and compared with experimental results. The icebreaking pattern of two different-shaped bows is realistically and accurately simulated in Section 6, which demonstrates the superiority of the proposed method in modelling the phenomenon of crack propagation over other numerical methods.

2. Ice model based on meshfree particle method

According to previous studies of ice mechanics (Derradji-Aouat, 2003; Palmer and Dempsey, 2009; Tippmann, 2011), ice is strain-sensitive material in various loading conditions. It exhibits the mechanical characteristics of ductility under low strain rate loading conditions, and it fails in the form of creep and microcracks instead of crack formation. Therefore, ice materials can be regarded as viscoelastic plastic materials at low strain rates (Jordaan, 2001; Molyneux, 2017). At high deformation strain rates, i.e., above ≈10^{-4}~10^{-3}, the cracks form and propagate in the ice body, typically an elastic and brittle process (Schulson, 1990; Schulson, 1999; Schulson, 2001). Normally, the ice is under the action of a high strain rate during the continuous icebreaking process (Derradji-Aouat, 2003; Gao et al., 2015; Molyneux, 2017). In other words, ice can be treated as elastic material and analysed with brittle failure mode when contacting ships. As a result, it is reasonable if the viscous-plastic deformation is not included in the process of ice-ship interaction, and the ice is modelled in the properties of PMB (Prototype Micro-elastic Brittle) for the simulation of ice-ship interaction (Ye et al., 2017). In the present work, the constitutive ice model is an isotropic, homogeneous PMB material established by ordinary state-based Peridynamics (OSB-PD).

In OSB-PD theory, ice is discretised into infinite material particles whose momentum information (e.g., force density) and motion information (e.g., displacement) can be integrated into the deformation and ice body's motion. Because the PD is a nonlocal method, the interaction exists between a particle and another particle in a certain range (H_x), which is usually called horizon. As shown in Fig. 1, the size of the horizon is δ.

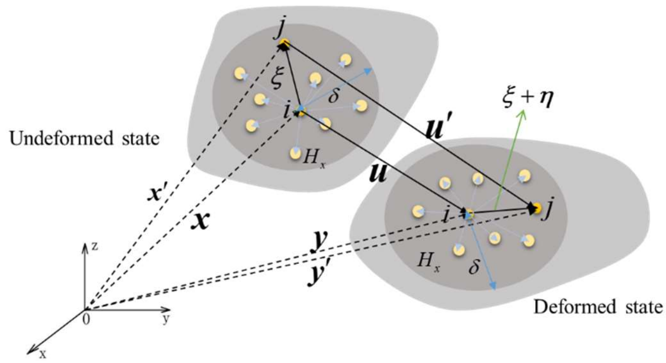

Fig. 1. Schematic diagram of particle interaction in PD theory

In the Cartesian coordinate system, the vector $\boldsymbol{x}$ represents the spatial position of the material point i, and it occupies a specific space volume V_x. Its density is expressed by $\rho(\boldsymbol{x})$. The material point j, interacting with i, is located by the vector $\boldsymbol{x}'$, as shown in the undeformed state in Fig. 1. When the ice body deforms, both particles i and j move to the new positions $\boldsymbol{y}$ and $\boldsymbol{y}'$ with displacement vectors $\boldsymbol{u}$ and $\boldsymbol{u}'$, as shown in the deformed state in Fig. 1. The force density of the particle i, which is viewed as the force exerted by the material point j, is stored in the state $\boldsymbol{T}$. The magnitude of the force density is unequal with the opposite direction directing to each other. It follows that the forces between two particles are two different force densities, which are $\underline{\boldsymbol{T}}[\boldsymbol{x},t]$ and $\underline{\boldsymbol{T}}[\boldsymbol{x}',t]$, respectively. The governing equation of the OSB-PD method is as follows (Madenci and Oterkus, 2014):

$$\rho(\boldsymbol{x})\ddot{\boldsymbol{u}}(\boldsymbol{x},t)=\int_{H_X}\left\{\underline{\boldsymbol{T}}[\boldsymbol{x},t]\langle \boldsymbol{x}'-\boldsymbol{x}\rangle-\underline{\boldsymbol{T}}[\boldsymbol{x}',t]\langle \boldsymbol{x}-\boldsymbol{x}'\rangle\right\}dV_{x'}+\boldsymbol{b}(\boldsymbol{x},t) \tag{1}$$

The constant parameters for PD can be derived by comparing the relation between strain energy density (a scalar-valued micropotential depends on the material properties as well as the stretch between a particle and all other material points in its family) and force density with the corresponding relation in classical medium mechanics (Madenci and Oterkus, 2014). Then, the detailed integral expression is derived by introducing these parameters into Eq. (1):

$$\rho(\boldsymbol{x})\ddot{\boldsymbol{u}}(\boldsymbol{x},t)=\int_{H_X}\left\{\frac{2\delta d\Lambda a}{|\boldsymbol{x}'-\boldsymbol{x}|}(\theta+\theta')+4\delta bs\right\}\frac{\boldsymbol{y}'-\boldsymbol{y}}{|\boldsymbol{y}'-\boldsymbol{y}|}dV_{x'}+\boldsymbol{b}(\boldsymbol{x},t) \tag{2}$$

In which, a 、d and b are PD constants, Λ is the auxiliary parameter, θ and θ' are volume expansions of current particle and its interacting particle in the horizon, respectively. s is the stretch between particles. $\boldsymbol{b}$ is the external force. Their expressions are as follows (Gao and Oterkus, 2019):

$$s=\frac{|\boldsymbol{y}'-\boldsymbol{y}|-|\boldsymbol{x}'-\boldsymbol{x}|}{|\boldsymbol{x}'-\boldsymbol{x}|} \tag{3}$$

$$\theta=\int_{H_X} d\delta s\Lambda dV \tag{4}$$

The stretch dominates the ice damage, as described in Ye et al. (2020). The interaction disappears when the stretch s exceeds the critical stretch s_0, which is an irreversible process. Therefore, it is reasonable to introduce a historical deformation state scalar Ω to represent the interaction between particles. $\Omega=0$ indicates no-interacting between particles while $\Omega=1$ represents that there still exists an interaction. The criterion in PD is expressed as follow:

$$\Omega(t,\xi)=\begin{cases}1 & \mathrm{s}(t',\xi)<\mathrm{s}_0\\ 0 & \mathrm{s}(t',\xi)\geq \mathrm{s}_0\end{cases} \tag{5}$$

The critical stretch value is:

$$s_0 = \begin{cases} \sqrt{\dfrac{G_c}{(3\mu + (\frac{4}{3})^4 (K - 2\mu))\delta}} & \text{for 3D} \\ \sqrt{\dfrac{G_c}{(\frac{6}{\pi}\mu + (\frac{16}{9\pi^2})(K - 2\mu))\delta}} & \text{for 2D} \end{cases} \tag{6}$$

where G_c is energy release rate, and can be expressed by fracture toughness K_I, that is $G_c = K_I{}^2/E$. K is bulk modulus. μ is shear modulus.

3. Fast contact detection algorithm (FCDA)

The hull is regarded as a rigid boundary wall in the contact process between ship hull and ice particles. It follows that particles would penetrate the hull in the collision process, which goes against the physical reality. Therefore, it is necessary to relocate and update the particles that have penetrated the hull surface, which involves contact detection between the hull surface and ice particles. The contact detection of PD particles impacting a regular-shaped rigid body, such as cylindrical surface, spherical surface, can be easily achieved by a simple mathematical algorithm based on the distance judgment between the particle and the object surface (Madenci and Oterkus, 2014). Moreover, it is also easy to relocate penetrated particles for regular-shaped impactors since any location on the surface of regular objects can be located by a simple geometric method. However, it is difficult to detect the contacting particles by the simple judgment criterion regarding the complex hull surface with typical and complicated curvature. Liu et al. (2018) discretised the hull surface into particle points and detected the contact process by judging the distance between ice particles and hull particles. By this method, the hull surface is supposed to be discretised into numbers of points to describe the outline of the hull bow accurately, which causes an increase in calculation consumption due to the heavy workload for particle search and motion integration. A more efficient contact detection algorithm, Point To Plane Distance Algorithm, was proposed by Vazic (2020), which can be used for a convex polyhedron with N faces. In the present work, the same basic theory is adopted and a fast contact detection algorithm (FCDA) based on a geometric algorithm is proposed to judge the contact process between ice particles and ship hull.

In the FCDA method, the hull is discretised into a series of quadrilateral planar elements sufficient to describe the hull surface's outline. Then the contact detection process between ice particles and hull can be simplified as a mathematical problem to judge the relative position of the material points and plane elements in space. The detailed FCDA scheme is introduced as the following steps, and the schematic diagram for the developed contact method is depicted from Fig. 2 to Fig. 6:

1) the ice material is discretised into particles, and the ship hull, which is simplified to a simple surface in diagrammatic sketches (Fig. 2 to Fig. 6), is divided into quadrilateral planes, and the schematic diagram of the initial model of ice particles preparing to contact with the rigid surface is shown in Fig. 2.

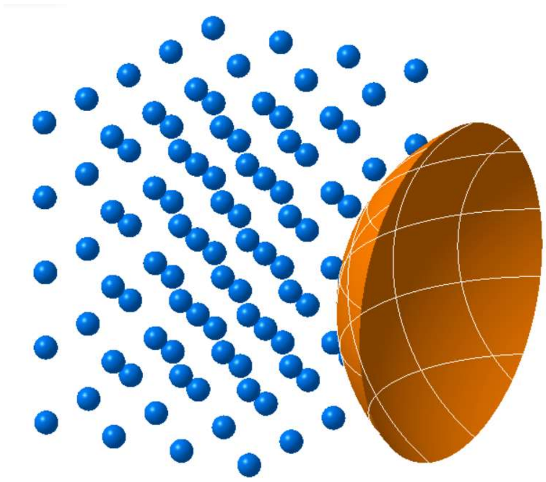

Fig. 2. Ice particles are going to penetrate the rigid surface (discretised into quadrilateral planar elements) in a 3-D view

2) The particles that are impossible to contact the surface at *t* time can be excluded before contact detection starts, which significantly reduces the number of particles that need to be searched and saves computational cost. For this purpose, a cube-bounding box containing the entire hull surface is established. The length, width, and height of the cube are equal to the maximum length, width, and height of the surface projected on the three coordinate

planes (length, breadth, and depth of the icebreaker). Accordingly, only the particles entering the bounding box may collide with the target surface. In this way, a large number of particles that are impossible to contact are excluded, and the search efficiency is improved, as shown in Fig. 3.

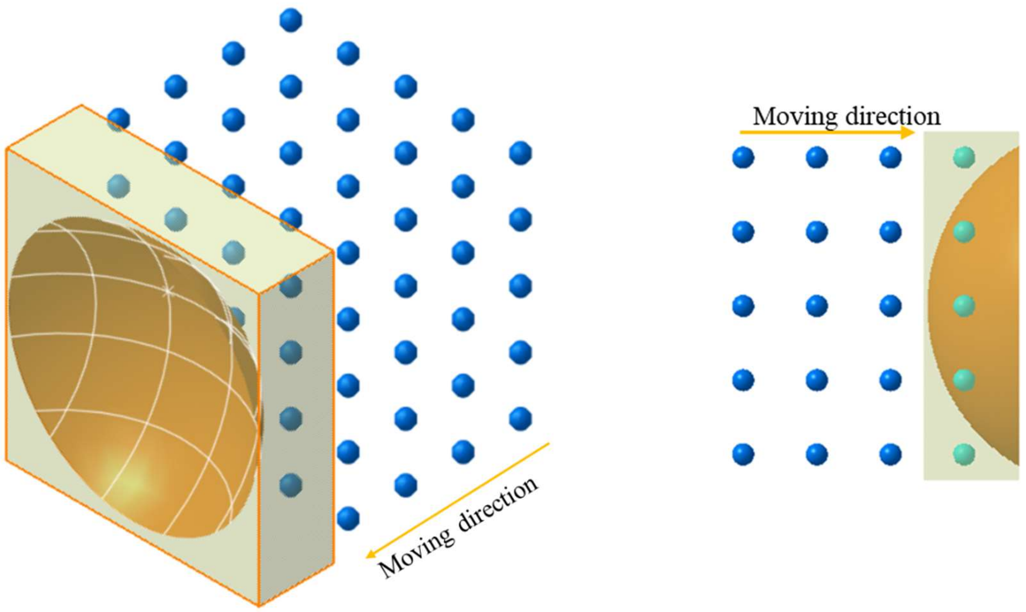

(a) (b)

Fig. 3. A bounding box containing the surface is established to exclude the particles that are impossible to contact the surface: (a) 3-D view; (b) profile view

3) At $t+\Delta t$, some ice particles penetrate the bounding box and the target surface, and only these particles need to be considered in the next step, as shown in Fig. 4.

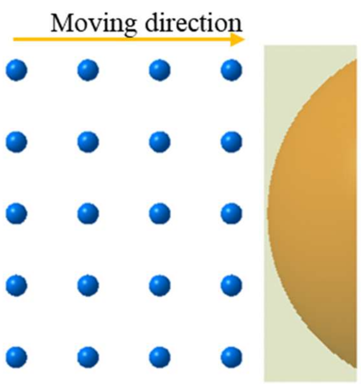

Fig. 4. Some ice particles penetrate the bounding box and the target surface

4) Before finding the unique plane that is contacted or penetrated by a particle, the possible planar elements impacting particles need to be determined first. Taking Fig. 5 as an example, it is noted that 25 particles are inside the bounding box, and 9 of these particles are possibly in contacting or passing through the target surface. The work should be done to identify these 9 particles and the planar elements they may penetrate. Taking the most intermediate particle as an example in Fig. 6, the method to determine the possible plane being penetrated by the particle is introduced in the fifth step.

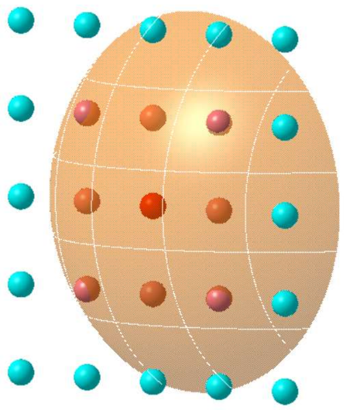

Fig. 5. All particles inside the bounding box are likely to contact the surface

5) Supposing that the coordinate of the particle is (x_0, y_0, z_0). As for all the quadrilateral planar elements on the target surface, the minimum and maximum values of the four corners in three directions can be determined, $(x_{\min}, y_{\min}, z_{\min})$ and $(x_{\max}, y_{\max}, z_{\max})$. If the relation between planar element and particle is $x_{\min} < x_0 < x_{\max}$ and $z_{\min} < z_0 < z_{\max}$ or $x_{\min} < x_0 < x_{\max}$ and $y_{\min} < y_0 < y_{\max}$, it is considered that these planes may collide with the particle, as shown in Fig. 6.

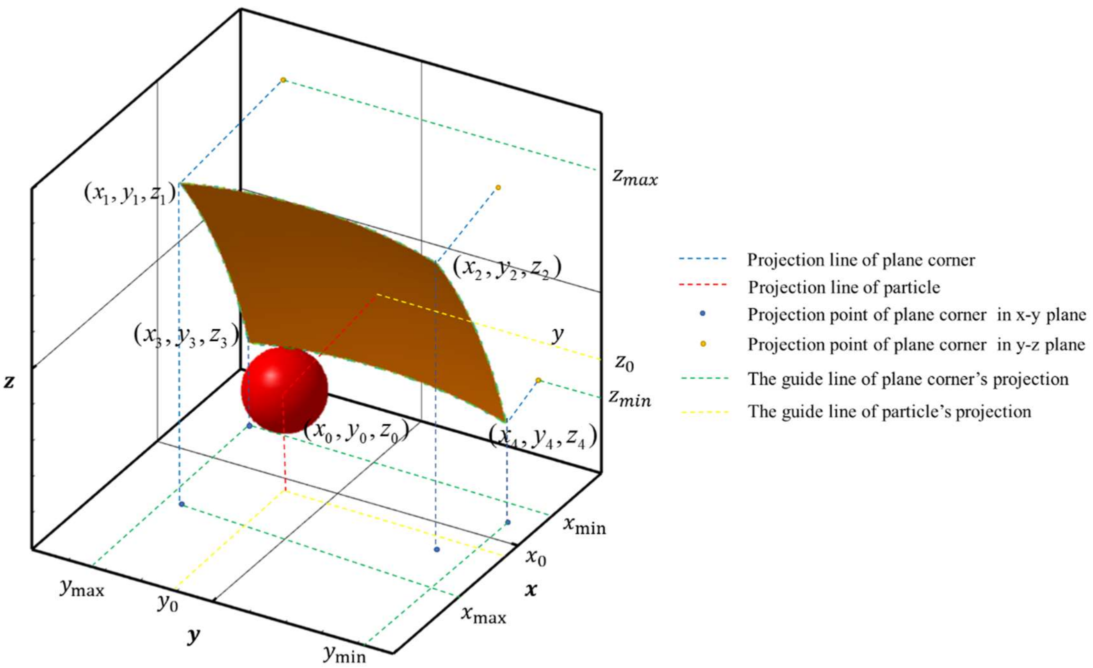

Fig. 6. Schematic diagram of searching for possible planar elements contacting with particle

6) The exact planar elements contacting the particle are completely determined at this step. Now, contact detection has been simplified as a mathematical problem of the relative position relationship between space point and plane. The equation of the plane $Ax + By + Cz + D = 0$ for each discretised hull element is established, and the distance formula between space point and plane is applied to relocate particles. Then, the final criteria for judging contact is as follows:

$$\begin{cases} Ax + By + Cz + D \geq 0 & \text{contact} \\ \text{Otherwise} & \text{no contact} \end{cases} \tag{7}$$

Then the relocation of the contacted particle is:

$$\boldsymbol{x}^{t+\Delta t} = \boldsymbol{x}^{t} + V_0 \cdot \Delta t + d \cdot \boldsymbol{n} \tag{8}$$

Wherein d is the distance between particle and plane. $\boldsymbol{n}$ is the normal vector of the plane, which is determined according to Vazic (2020).

The velocity of the redistributed particle in its new location is calculated as:

$$\boldsymbol{v}^{t+\Delta t} = \frac{\boldsymbol{u}^{t+\Delta t} - \boldsymbol{u}^{t}}{\Delta t} \tag{9}$$

The force exerted on the target by the contact particle i is:

$$F_{(i)}^{t+\Delta t} = -1 \times \rho_{(i)} \frac{v_i^{t+\Delta t} - v_i^t}{\Delta t} V_{(i)} \tag{10}$$

Summation of the contributions of all contacted material points results in the total reaction force, that is:

$$F_{total}^{t+\Delta t} = \sum_{i=1} F_{(i)}^{t+\Delta t} \lambda_{(i)}^{t+\Delta t} \tag{11}$$

Where $\lambda_{(i)}^{t+\Delta t}$ indicates the contact state between particles and structure, and is：

$$\lambda_{(i)}^{t+\Delta t} = \begin{cases} 1 \text{ inside structure} \\ 0 \text{ outside structure} \end{cases} \tag{12}$$

4. MPI parallel scheme

The most commonly used parallel technology for the PD framework is the OpenMP programming method based on the multi-threaded, shared memory parallelism mode (Prakash and Stewart, 2020). OpenMP features simplicity, time saving, and easy to achieve since the calculation domain can be automatically divided into multiprocessors with only a few directives instructing the parallel computing. Corresponding to its advantages, the disadvantages of this method are also apparent: It is limited by the computer's thread and physical memory in numerical computation of a large amount of data. Besides, data competition may occur when the calculation domain is unevenly decomposed or the computational efficiency of each thread is uncontrollable. Parallelisation at different threads needs to be completed simultaneously to ensure the synchronous state of the numerical calculation, which may consume computing time. Furthermore, the OpenMP is a parallel computing mode of shared memory that always leads to computing overflow in moderate to large problems.

MPI is a kind of message-passing programming model that requires higher compilation skills for researchers to analyse numerical procedures and build the optimal parallel algorithm. Moreover, it is not easy to debug for MPI. However, this parallel technology is a distributed parallel method with high scalability, realising a high-performance parallel calculation of the cluster and reducing a single computer's hardware requirements. Furthermore, MPI implementation is a substitutional method to overcome computing overhead by passing considerable information between threads. In this paper, the OSB-PD program is compiled based on MPI, which can realise the calculation of a large amount of data on the hardware of small memory and provide the basic technical support for high-performance calculation in the future.

The computational cost of the PD method is mainly consumed in the calculation loop of the particles in the problem domain, which means the more particles in the model, the greater consumption of computation. Therefore, the best strategy for saving computing time is to reduce the computational complexity in numerical particle integration. This can be solved by multiple processors sharing the total numbers of particles, in other words, the domain decomposition algorithm (Cui et al., 2020). In order to achieve the parallelisation of level ice-ship interaction, the level ice (computing domain) discretised into numbers of particles are decomposed into np processors, for example $np = 9$, as shown in Fig. 7.

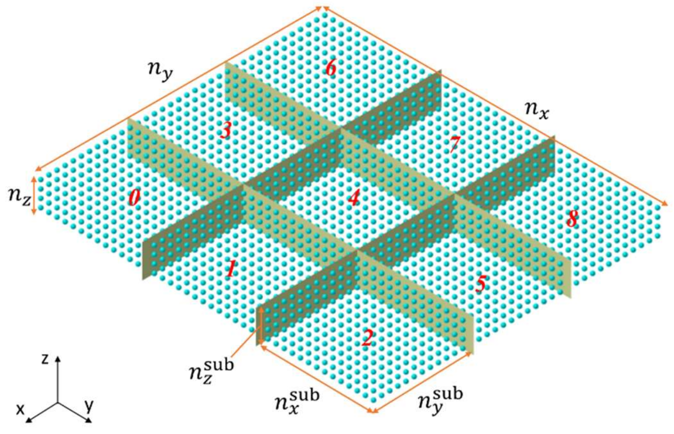

Fig. 7. The discretised ice sheet is decomposed into 9 processors numbered from 0 to 8

In Fig. 7, considering the length and width of the ice layer are much larger than the thickness, the calculation domain is divided into 9 parallel threads (the number of processors can be determined according to the configuration of the computer) on the *x*-*y* plane where the ice layer lies on. And they are numbered from 0 to 8, in which thread 0 is the primary processor. The number of particles at the level ice in three directions is n_x , n_y , and n_z , respectively. And the number of particles in the three directions after dividing by each processor is n_x^{sub} , n_y^{sub} ,

n_z^{sub}, respectively, wherein $n_z^{sub} = n_z$ since particles along thickness direction are decomposed into one thread. Therefore, the total particle number in each processor is $ntot = n_x^{sub} \cdot n_y^{sub} \cdot n_z$.

In the PD method, each particle interacts with particles in the horizon $\delta = m \cdot dx$, wherein, dx is the particle spacing and m is a positive integer representing the multiple relationships. With this in mind, although particles along the thread boundary are in different processors (as shown in Fig. 8), they are still needed to be included with the current thread when calculating since they are in the horizon of current particles. These particles participate in the integral process of the thread they are in and the numerical integral process in adjacent threads. Accordingly, we call these particles in overlapping computing domains exchange particles since their information needs to be sent to neighbor threads. Take thread 4 as an example; as shown in Fig. 8 (a top view of Fig. 7), all particles that interact with particles in thread 4 are located in the black dotted box. It can be seen that part of family members is decomposed in the other threads (0, 1 2, 3, 5, 6, 7, and 8 respectively) when assuming that $m = 3$. Consequently, the maximum number of particles that each thread needs to hold is:

$$ntotm = ntot + n_x^{sub} \cdot n_z \cdot 2 + n_y^{sub} \cdot n_z \cdot 2 + n_z \cdot 3 \cdot 3 \cdot 4 \tag{13}$$

as shown in Fig. 9 (particles in the black dotted box of Fig. 8).

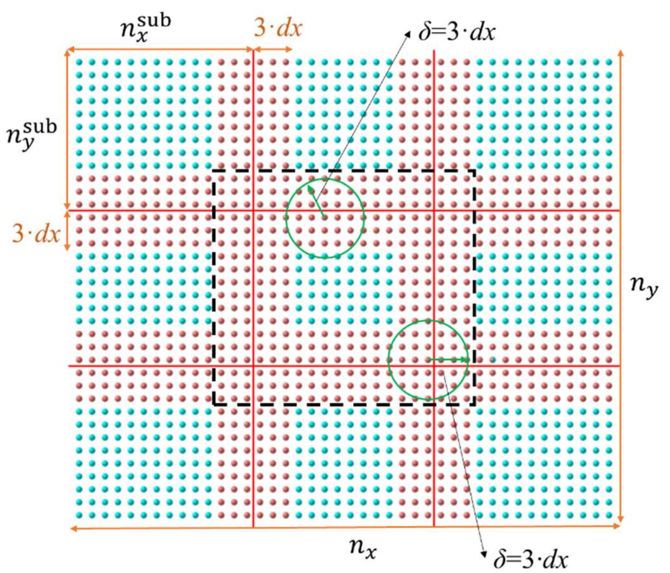

Fig. 8. An explanatory diagram of the situation where there are particles information exchange between

threads (A top view of Fig. 7)

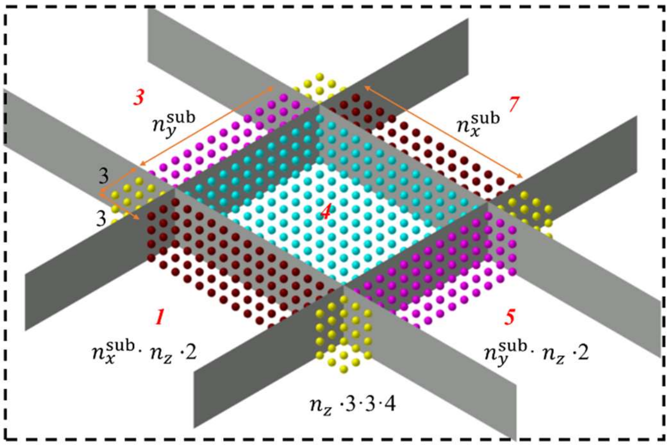

Fig. 9. Interpretation diagram for counting the maximum number of particles to be processed by each thread (particles in the black dotted box of Fig. 8)

So far, the critical issue of calculation domain decomposition in parallel computing has been solved. The rest is to apply the standard directives of MPI to perform numerical integration of particles in each thread. It is noted that particles' information in overlapping computing domains should be transferred to adjacent threads by sending and receiving directives at each time step.

5. Solution strategy for ISI and its implementation in MPI parallel scheme

The developed model in the present work is programmed in FORTRAN language with the MPICH implementation platform. The numerical strategy for FCDA is first analysed in Section 5.1, followed by an implementation demonstration of the ISI model in Section 5.2. Then, the framework of the MPI scheme is designed in Section 5.3.

5.1. Numerical implementation for FCDA

The solution procedure for FCDA follows the steps below:

(1) at the $t + \Delta t$ time step, initialise arrays of particle coordinates at the current time step $coord^{t+\Delta t}(x, y, z)$,

at t time step $coord^{t}(x,y,z)$, and the new position after relocation $relo^{t+\Delta t}(x,y,z)$, respectively. Initialise the pointer used to represent the penetration: $kpp=0$.

(2) Judge whether particles enter the bounding box, Ω_{bb}, mentioned in the second step in Section 3. We can achieve this step by checking the *x* and *y* coordinates of ice particles since there are only a few discretisations in the *z*-direction of ice and ship models. If $coord^{t+\Delta t}(x,y)$ is inside the bounding box, that is $coord^{t+\Delta t}(x,y)\subseteq\Omega_{bb}$, then $kpp\leftarrow 1$ else $kpp\leftarrow 0$. The algorithm for this step is as follows:

Algorithm 1: Determine the particles inside the bounding box

Input location of the bounding box in the *x*-*y* plane: $\mathrm{x\,min\,box}$, $\mathrm{x\,max\,box}$, $\mathrm{y\,min\,box}$, and $\mathrm{y\,max\,box}$

for each particle of the ice model **do**

if ($\mathrm{x\,min\,box}\le coord^{t+\Delta t}(x)\le \mathrm{x\,max\,box}$) and ($\mathrm{y\,max\,box}\ge coord^{t+\Delta t}(x)\ge \mathrm{y\,min\,box}$) **then**

$kpp\leftarrow 1$

else

$kpp\leftarrow 0$

end if

end for

---

(3) If $kpp=1$, find the possible particles that may contact with hull by the method described in step 4 and step 5 in Section 3. The algorithm for this step is:

Algorithm 2: Find the possible particles that may contact the hull

---

for each quadrilateral planar elements of the ship model **do**

update coordinates of 4 corners from last time step

Calculate the minimum and maximum coordinate: $x\min$, $x\max$, $y\min$, $y\max$

if ($coord^{t+\Delta t}(x) \le x\max$) and ($coord^{t+\Delta t}(x) \ge x\min$) and ($coord^{t+\Delta t}(y) \le y\max$) and ($coord^{t+\Delta t}(y) \ge y\min$) **then**

Calculate the pointer $kship$ which judging whether the particle is inside the hull elements by a subroutine which is produced in step (4)

update pointer kpp

else

$kpp \leftarrow 0$

end if

end for

---

(4) Among possible particles found at the previous step, determine particles that contact the hull (inside the hull element) according to the criterion proposed in step 6 in Section3. The algorithm for this step is:

Algorithm 3: Determine the particles that are inside hull elements

---

for each possible contacting particle P **do**

for each quadrilateral planar element (with 4 corners A, B, C, D) of the ship model **do**

Calculate two intersecting vectors $\boldsymbol{AC}$ and $\boldsymbol{BD}$ on the plane

Calculate Normal vector of the plane by $\boldsymbol{n} \leftarrow \boldsymbol{AC} \times \boldsymbol{BD}$

Calculate the plane equation $Ax + By + Cz = D$

Substitute P coordinate (x_0, y_0, z_0) into $Ax + By + Cz = D$,

$val \leftarrow Ax_0 + By_0 + Cz_0 + D$

if $val \ge 0$ **then**

$kship \leftarrow 1$

Calculate distance between P and plane $ABCD$

Relocate position of P $relo^{t+\Delta t}(x, y, z)$ by Eq. (8)

else

$kship \leftarrow 1$ and $kpp \leftarrow 0$

end if

end for

end for

---

(5) Then the pointer $kship \leftarrow 1$, and the new position $relo^{t+\Delta t}(x, y, z)$ of the relocated particle are returned to the main program, further analysed in Section 5.2, to calculate the contact force $penF(x, y, z)$ and acceleration of particles. The contact force calculation is not elaborated here since it has been suggested in chapter 10 of Madenci and Oterkus (2014) using a rigid contact model.

5.2. Numerical implementation for ISI

The numerical procedure for ISI is implemented in a gaussian meshless scheme, in which the ice body is discretised into uniformly distributed particles. Please note that the surface effects caused by the free surface of interaction and volume correction needed due to incorrect volume integration in the PD theory are included in the implementation according to the numerical solution proposed in Madenci and Oterkus (2016), and boundary conditions are imposed according to study in Oterkus et al. (2014).

Moreover, the determination of the family member is a time-consuming process, as analysed in Vazic et al. (2020). Hence, a more efficient method needs to be explored to search for family members. In this study, the Link-list algorithm (Monaghan, 1985), which is originally used in the SPH method, is applied to determine the array of family members. Link-list search algorithm divides interest domain into numbers of regions by grid. When determining the family of the particle, only the grid, in which the particle is located, and its neighbouring grids need to be searched. As a result, the computational cost of the family search process is greatly reduced by utilising the

Link-list algorithm.

The main part of the ISI is the PD equation, which is solved by spatial integration, and FCDA is packaged as a callable submodule when it goes to the contact process. The framework of ISI follows the below steps:

1) Input ship model, calculation conditions and ice geometries. Initialise variables and arrays.
2) Discretisation of the ice sheet
3) Construction of particles in the horizon region
4) Surface correction
5) Time integration, including
   (1) Boundary condition
   (2) Loop for dilatation calculation
   (3) Loop for PD force calculation
   (4) Loop for accretion update
   (5) Loop for contact process using FCDA
6) Out

The flowchart of ISI is shown in Fig. 11 in the solid box.

5.3. ISI in MPI parallel scheme

We performed numerical simulation on a computer with 16 threads. Therefore, the calculation domain is partitioned into $np = 15$ processors. Considering that the model length of the ice sheet is larger than the width, there are 5 threads in the length direction and 3 in the width direction, as shown in Fig. 10. Moreover, the necessary procedure for parallel is the communication of particles' information in overlapping computing domains after each calculation step relating to the interaction between two particles. This is instructed in the flowchart, as shown in Fig. 11 with dashed boxes.

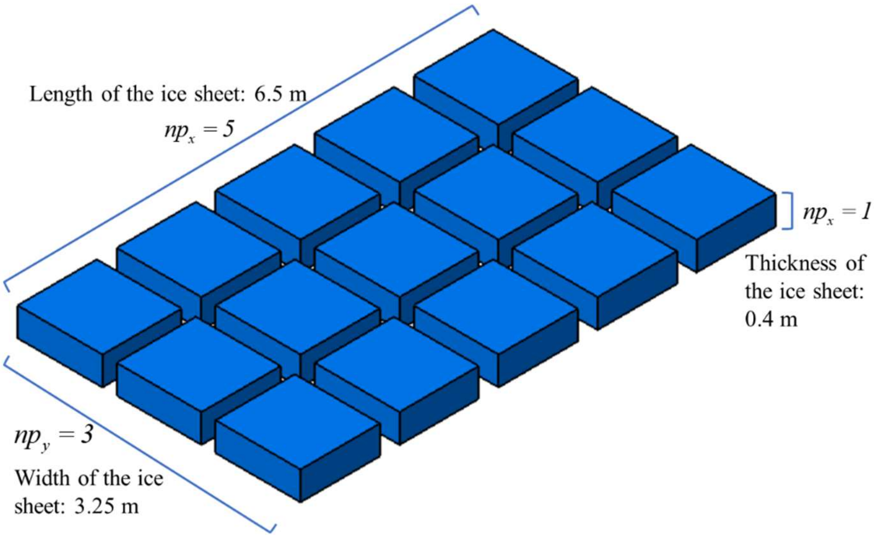

Fig. 10. Partition of the computing domain for ice sheet

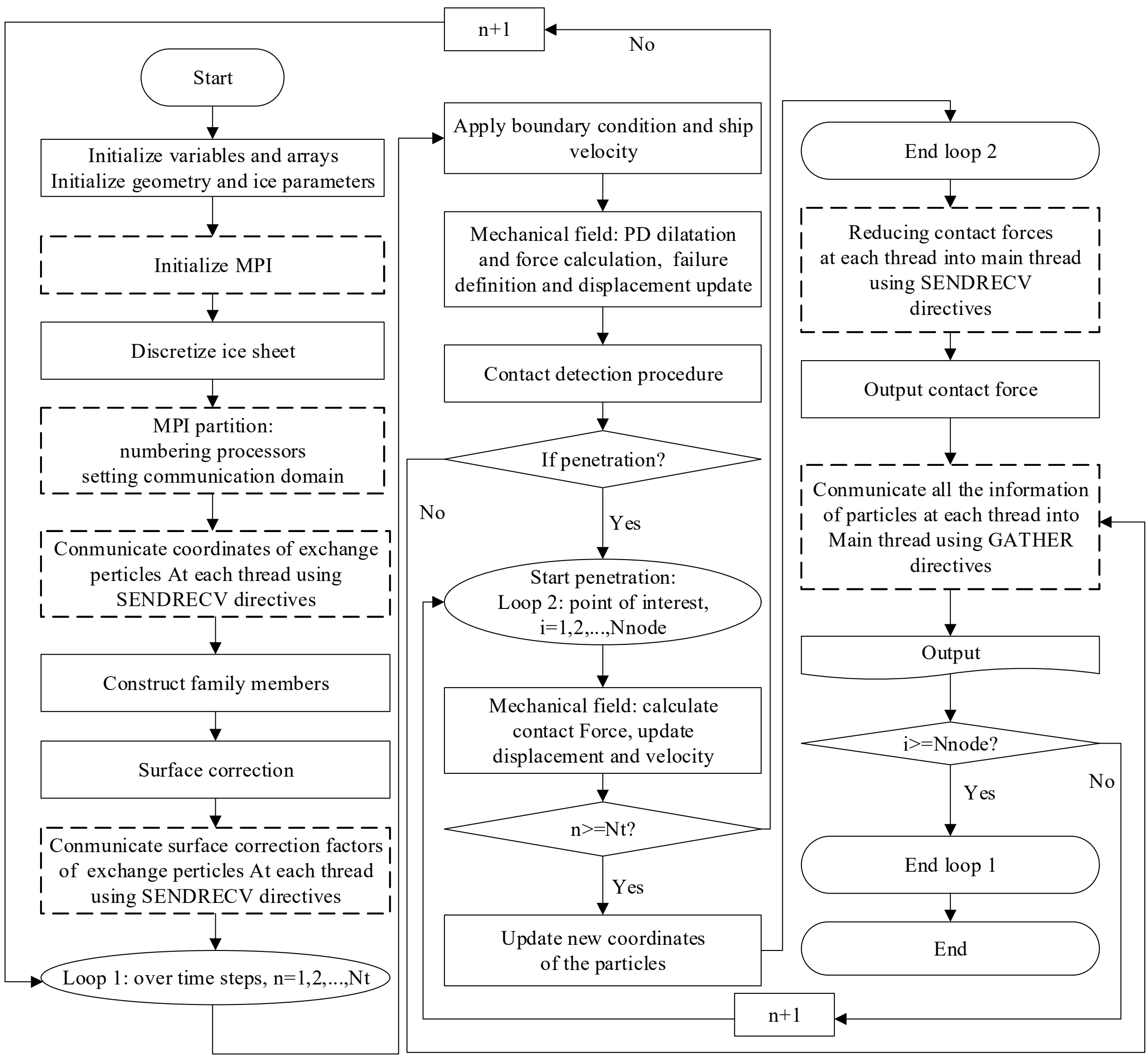

Fig. 11. The schematic for ISI in MPI parallel scheme

6. Numerical simulation of two different-shaped bow breaking level ice

In this section, the numerical models of conventional and unconventional icebreaker bows breaking level ice are established based on the above-developed method. Then, the icebreaking pattern and icebreaking loads are predicted and compared with existing experimental results, which illustrates the model's effectiveness in the present paper. Comprehensive verification of the numerical model has also been carried out by comparing the icebreaking resistance with different ship velocities obtained from the present numerical simulation to the experimental measurements (Zhang et al, 2021). Furthermore, the analytical study is carried out to discuss the differences in the icebreaking process between two different bow shapes.

6.1. Model set up

The selected conventional bow is a straight stem bow with paralleled buttock lines, which originated from Soviet and Finnish icebreakers in 1950. This kind of type has an extreme (sharp and thin) icebreaking bow and is excellent in breaking the ice (Park et al., 2007). It is still widely used and regarded as a parent bow for icebreaker design. The simplified Thyssen WAAS bow is selected as the unconventional icebreaker in the present work (Puntigliano, 1995). This kind of bow has different characteristics compared with the traditional bow (Sodhi, 1995): the bow shows a moderate shape line and is especially excellent in ice removal ability, according to model study in Freitas and Nishizaki (1986). The main characteristics of two different icebreaker bows are shown in Fig. 12.

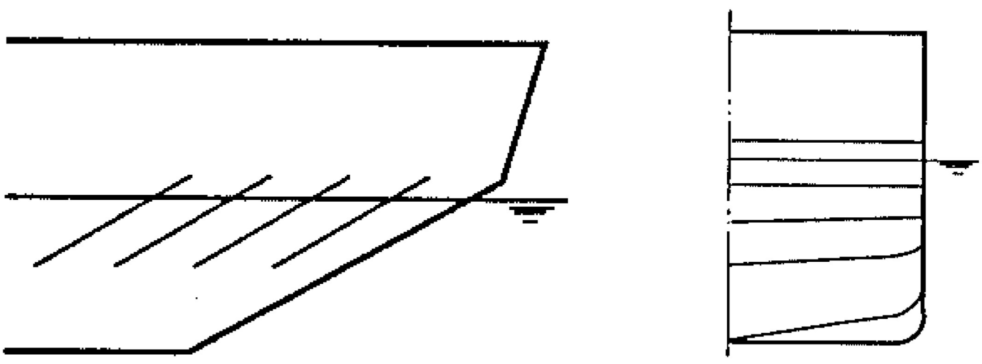

Straight stem with parallel buttocks — Thyssen-WAAS bow

Fig. 12. Shapes of two different icebreaker bow (Sodhi, 1995)

The principal dimensions of the two icebreaker bows are shown in Table 1. Please note that the scale ratio of $1:25$ is set. Fig. 14 gives the 3-D model of the icebreaker bow.

Table 1 Principal dimension of two kinds of icebreaker

Items	symbol/unit	Conventional bow		Unconventional bow	
		Full scale	Model scale	Full scale	Model scale
Length between perpendiculars	$L_{\mathrm{pp}}/\mathrm{m}$	147.2	5.888	100.0	4.0
Breadth	B/m	23.0	0.92	20.0	0.8
Depth	D/m	13.5	0.54	12.0	0.48
Draft	T/m	8.0	0.32	7.0	0.28
Flare angle	φ/deg	33	33	77	77
Waterline angle	α/deg	22	22	39	39
Buttock angle	ψ/deg	28	28	13	12
Stem angle	β/deg	24.35	24.35	14	14
Bow length	$L_{\mathrm{f}}/\mathrm{m}$	32.5	1.3	10.0	0.4

The four characteristic angles describing the bow shape of the icebreaker in Table 1 are illustrated in Fig. 13.

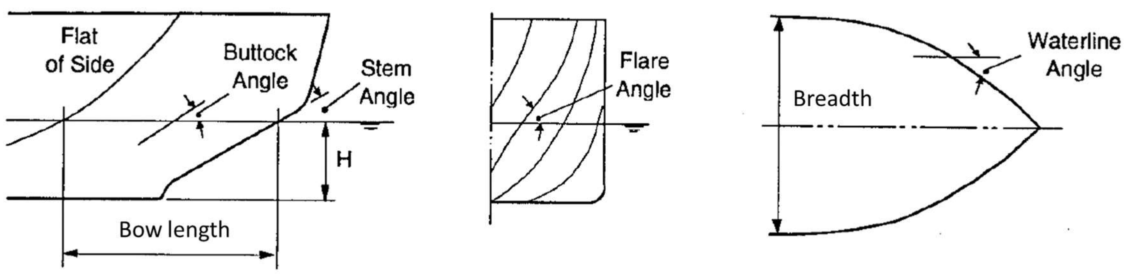

Fig. 13. Main characteristic angles of bow forms (Sodhi, 1995)

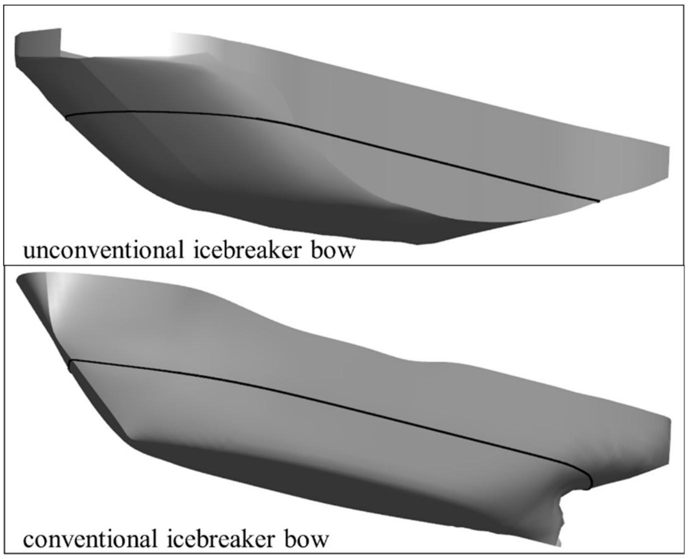

(a) 3-D view

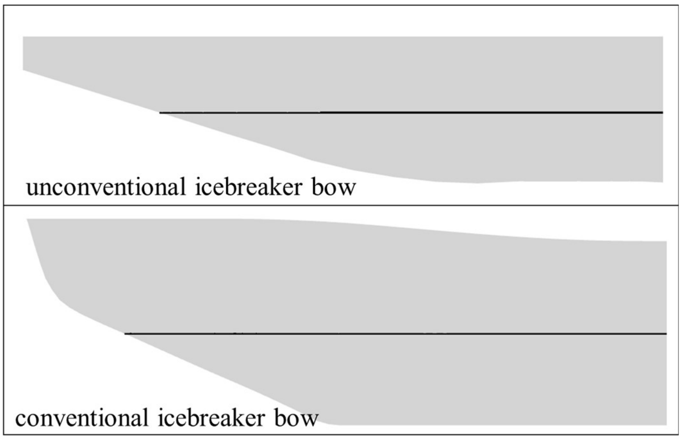

(b) profile

Fig. 14. The models of two icebreakers. The line on the hull is the waterline

As for the ice material parameters, shown in Table 2, the ice engineering properties are set to be the same with a model test used to verify the effectiveness of the present method, as shown in Section 6.2. Model-I fracture toughness of ice is given as $60\text{kPa}\cdot\text{m}^{0.5}$ (Vazic et al., 2019). Moreover, the condition information and discretisation are also illustrated in Table 2. The critical stretch is calculated according to Eq. (6). Particle space is discretisation size, that is, the distance between particles. The horizon described in Section 2 is three times the particle space. It is noted that the right and left sides along the forward direction of the ice model are set to be fixed boundaries.

Table 2 Calculation parameters of the model

Ice properties	**symbol/unite**	**value**
Density	$\rho/\mathrm{kg/m^3}$	826.6
Elastic modulus	$E/\mathrm{P_a}$	52.0E6
Poisson's ratio	ν	0.33
Fracture toughness	$K_I/\,\mathrm{kPa\cdot m^{0.5}}$	60
Critical stretch	s_0	0.0052
Numerical setup	**symbol/unite**	**value**
Timestep	dt/s	2.0E-5
Particle space	dx/m	0.013
horizon	δ/m	0.39
Condition information	**symbol/unite**	**value**
Thickness of the ice sheet	$T_{\mathrm{ice}}/\mathrm{m}$	0.4
Length of the ice sheet	$L_{\mathrm{ice}}/\mathrm{m}$	6.5
Width of the ice sheet	$B_{\mathrm{ice}}/\mathrm{m}$	3.25
Speed of the icebreaker	V_{bow}/kn	0.6

6.2. A verification with experiment

A series of model tests of icebreakers breaking the level ice were conducted in an ice tank at the Ice Engineering Laboratory of Tianjin University. The conventional bow is one of the models in the experiment, which followed the test procedure in Huang et al. (2018) and Huang et al. (2016). The verification is made by comparing the icebreaking pattern between experimental results and numerical simulation. Then the icebreaking load is predicted and converted into the full-scale data according to the reduction formula presented by ITTC (ITTC, 2017) to be compared to experimental data and Lindqvist's empirical result (Lindqvist, 1989). Comparison of icebreaking modes and icebreaking loads are shown in Fig. 15 and Fig. 16, respectively.

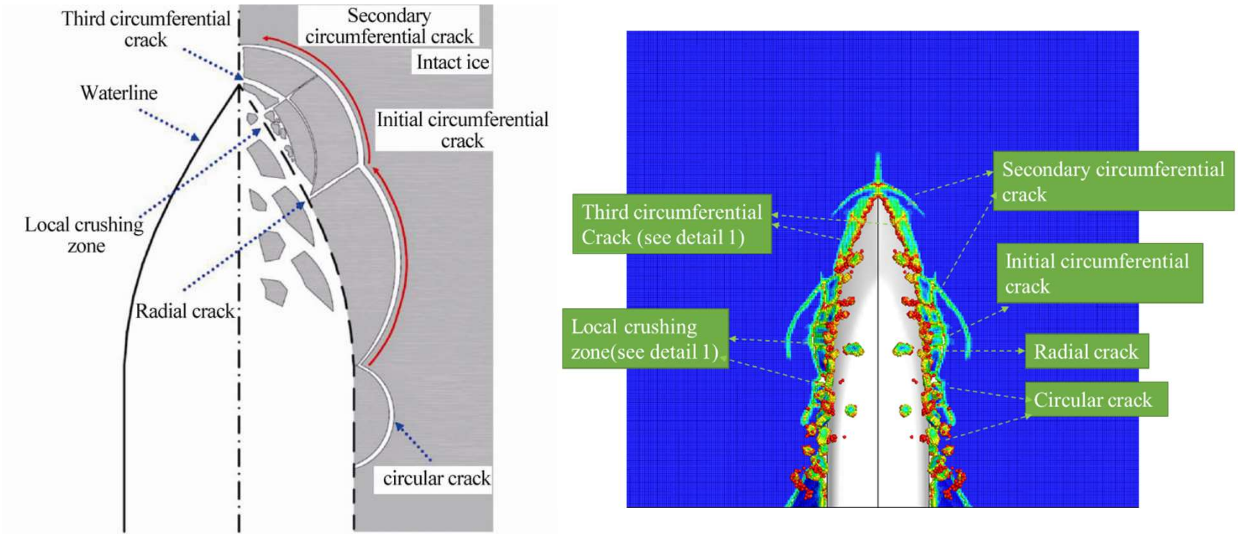

(a) The schematic diagram for the experiment (Huang et al., 2016) (b) Snapshot for numerical simulation form top view

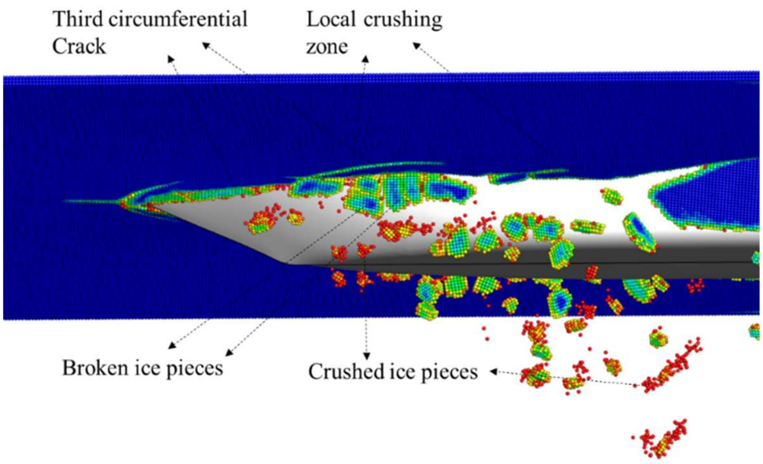

(c) Snapshot of detail 1 in (b)

Fig. 15. Comparison snapshot of icebreaking pattern verification（conventional bow with a speed of 2.058 m/s）

It is noted that the fluid mechanics and ice buoyancy have not been considered in the present model, some of the broken ice floes appear sinking and moving away from the hull. From the icebreaking pattern of the ice layer, the bending failure is the dominant damage mode that occurs accompanying the formation and propagation of circumferential cracks. The ice damage process at each icebreaking cycle is concluded as following steps:

1) Circumferential cracks along the hull side in length direction are generated and continues to expand on both sides of the bow. This type of crack forms at the position of half the width of the bow;

2) With the ship advancing, circumferential cracks propagation travels to the shoulder, and at the same time, radial cracks generate at the near position of the half-width of the bow;

3) The secondary annular cracks that are approximately parallel to the edge of the bow start and expand, accompanied by localised ice crushing and breaking;

4) Simultaneously, the short third circumferential crack begins to propagate at the bow.

The icebreaking pattern observed and analysed in the experiment is well captured by numerical simulation, verifying the effectiveness of the method in modelling ice damage and cracks propagation.

In this paper, the comparison of ice loads is made by the mean value of the numerical simulation, model test data, and the Lindqvist method. The most widely used approach, Lindqvist method, is selected to calculate the empirical result. Lindqvist (1989) divided the ice resistance into two main components, i.e., ice breaking and submersion of the ice floes. The resulting ice resistance is an empirical combination of the two components dependent on ship speed. The breaking component is expressed as follows:

$$R_{br} = (R_C + R_B)\cdot(1+\frac{1.4V}{\sqrt{gh_i}}) \tag{14}$$

in which:

$$R_B = \frac{27}{64}\cdot\sigma_f\cdot B\cdot\frac{h_i^{1.5}}{\sqrt{\frac{E}{12(1-\upsilon^2)g\rho_w}}}\cdot(\tan\omega+\frac{\mu\cos\phi}{\cos\omega\sin\alpha})\cdot(1+\frac{1}{\cos\omega}) \tag{15}$$

$$R_C = 0.5\sigma_f h_i^2\cdot\frac{\tan\phi+\mu_f\frac{\cos\phi}{\cos\omega}}{1-\mu_f\frac{\sin\phi}{\cos\omega}} \tag{16}$$

$$\omega = \arctan\frac{\tan\varphi}{\sin\alpha} \tag{17}$$

where R_B is the bending resistance, σ_f the flexural strength, B the ship breadth, h_i the ice thickness, υ the Poisson's ratio, ρ_w the density of water, g the gravitational acceleration, ω the normal angle, μ_f the friction coefficient between ship hull and ice, R_C the crushing resistance. The normal angle is calculated from the waterline entrance angle and the stem angle according to Eq. (17).

The average value of numerical calculation, experimental result, and the empirical result of icebreaking force in the prototype are 0.969 MN, 1.124 MN, and 1.1175 MN, respectively, as shown in Fig.16. The Lindqvist-breaking force refers to the icebreaking component in the Lindqvist approach (Lindqvist, 1989). The simulation calibrates with the experimental result. It can be concluded that the numerical calculation results are in good agreement with the experimental results and the empirical formula results.

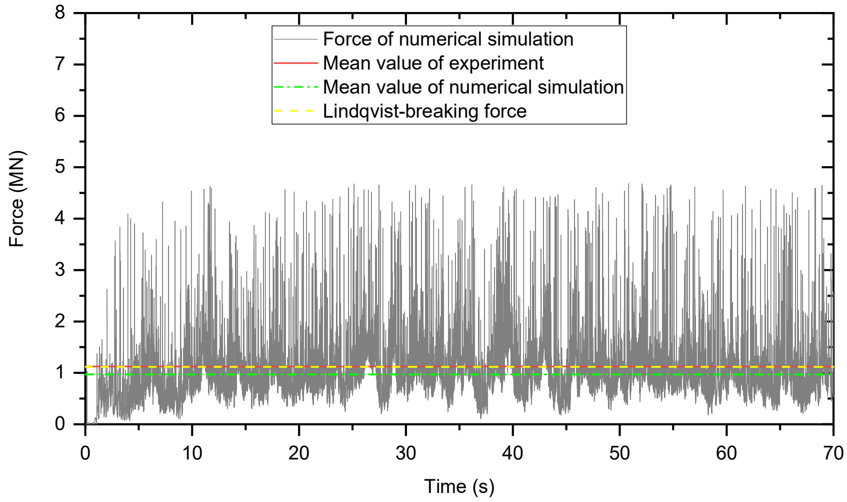

Fig. 16. Icebreaking resistance verification comparison (conventional bow with speed of 4 knots)

6.3. Icebreaking pattern comparison of two different-shaped bows

When the icebreaker navigates in level ice, different ice failure modes may occur according to ice condition, hull geometry: crushing, bending, buckling, splitting, or mixed-mode, where two or more failure modes are active at the same time (Lubbad and Løset, 2011). The damage caused by bending is the most control failure mode among these modes (Riska, 2010). The following case study supports the characteristics, as mentioned above, of the icebreaking process and shows that the hull form has a strong influence on the crack propagation and ice failing mode.

The icebreaking processes of the conventional bow and the unconventional bow step by step are analysed in

Table 3, which demonstrates the different crack propagation patterns, crack initiation location, ice failure mode, and channel edge between two bows. According to the crack initiation and propagation, both icebreaking processes are described as three steps, which are initial contact, crack initiation, crack propagation. Their ice-bow contact snapshots from Fig. 17 to Fig. 22 of the numerical simulation are also listed in corresponding steps in Table 3, in which the bow bodies are set to be transparent to achieve a better observation.

Table 3 A comparison of the icebreaking pattern (the numbers 1, 2, and 3 represent three stages, initial contact, crack initiation, and crack propagation, respectively. S and D refer to similarities and differences, respectively).

<table>
<tr><th></th><th></th><th>Conventional bow</th><th>Unconventional bow</th></tr>
<tr><td rowspan="2">1</td><td>S</td><td colspan="2">At the first stage, the icebreaker bows contact the free ice edge, and the single contact area is generated. This makes an opening on the contact area, and the local ice crushing is the dominant failure mode in both cases. However, the breaches present different shapes consistent with their bow profiles, as shown in Fig. 17 and 18, respectively.</td></tr>
<tr><td>D</td><td>The crushing area of contacting ice for the conventional bow is triangular, and one of the angles is about twice the water line angle. Simultaneously, it is noticed that the broken ice cusp is created by bending failure on both sides of the bow, which is also observed in the experiment (Huang et al., 2016).</td><td>The crushing area of contacting ice for the unconventional bow is circumferential, and the opening edge approximately agrees with the bow outline. At this stage, no apparent broken ice cusp formed. The opening width is larger than that of the conventional bow.</td></tr>
</table>

<table>
<tr><td></td><td></td><td>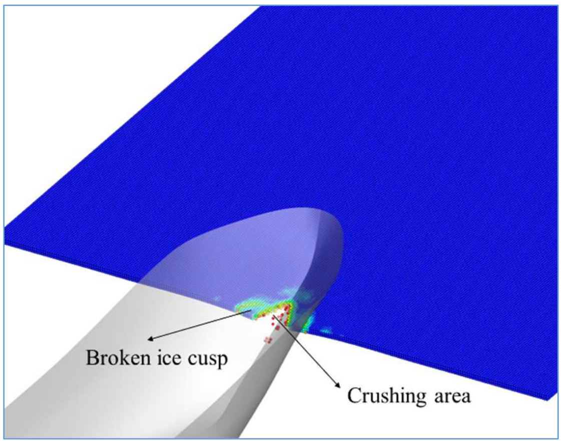

Fig. 17. Initial contact of the conventional bow</td><td>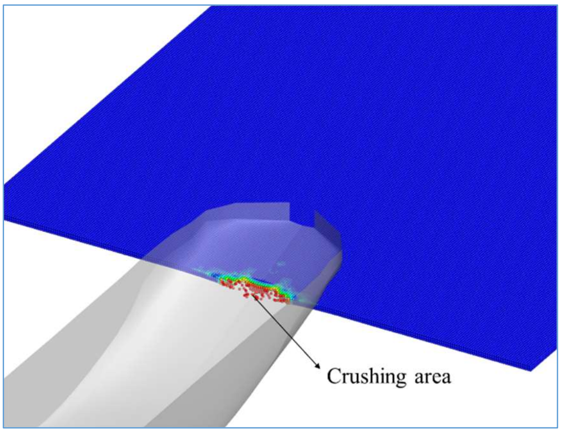

Fig. 18. Initial contact of the unconventional bow</td></tr>
<tr><td rowspan="2">2</td><td>S</td><td colspan="2">The crushing area increases as the bow penetrates the ice. This increase is ended by the circumferential crack initiation from both sides of the bow. Bending failure of the ice is observed.</td></tr>
<tr><td>D</td><td>The initial circumferential cracks, paralleling the waterline edge, start at the free edge of the ice sheet and travel to the stem. Consequently, two large broken ice pieces on the bow port and starboard generate due to bending failure.
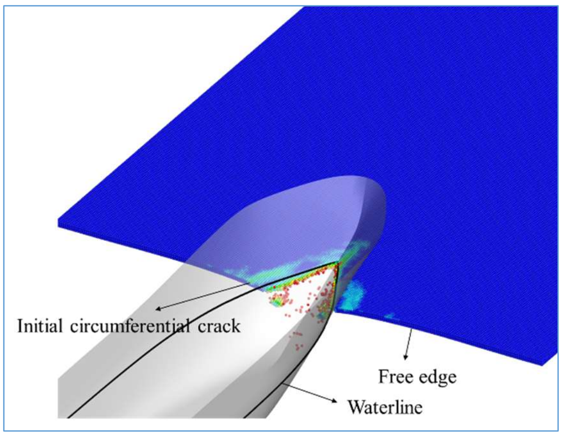

Fig. 19. Initial crack of the conventional bow</td><td>The weight of the bow bends the ice to ultimate failure, then circumferential cracks with waterline shape start from the free edge about the symmetrical position of the middle longitudinal profile. Two cracks meet at the stem and form into one crack.
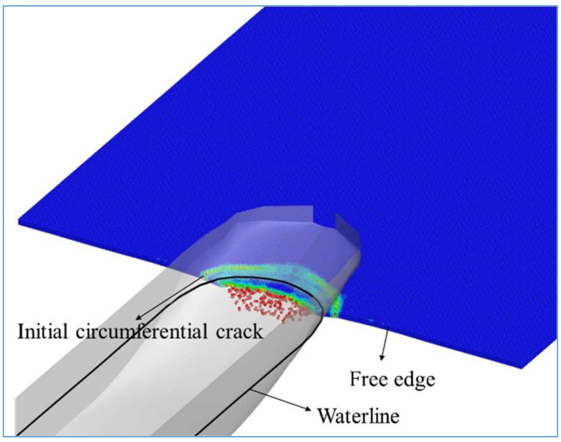

Fig. 20. Initial crack of the unconventional bow</td></tr>
<tr><td>3</td><td>S</td><td colspan="2">——</td></tr>
</table>

<table>
<tr>
<td rowspan="2"></td>
<td rowspan="2">D</td>
<td>The crack propagation is described from step (2) to step (4) in Section 6.2, and the following snapshots show these processes. With the ship moving, the ice area around the bow is always accompanied by crushing failure.</td>
<td>The radial cracks form from the contact area to the initial circumferential. The radial cracks near the middle of the ship begin to expand first, then the other radial cracks begin to expand until the ice region between the initial circumferential crack and the hull is completely broken. In crack propagation, there is almost no crushing failure since the ice has been bent before that.</td>
</tr>
<tr>
<td>
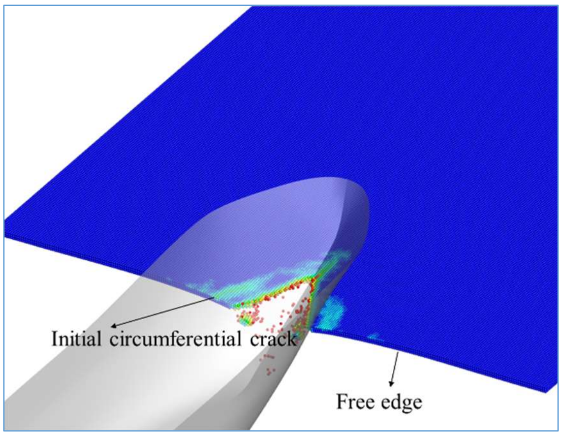

(a)
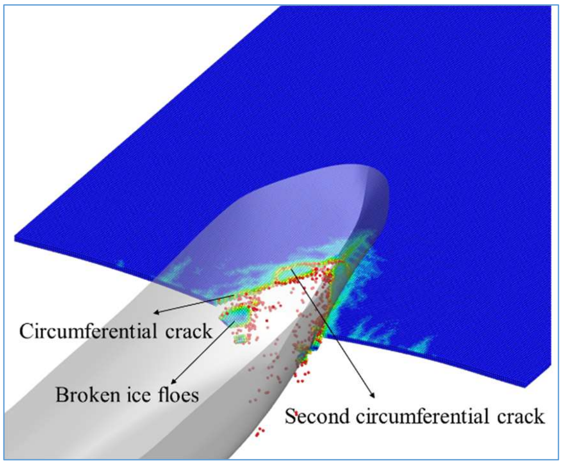

(b)
</td>
<td>
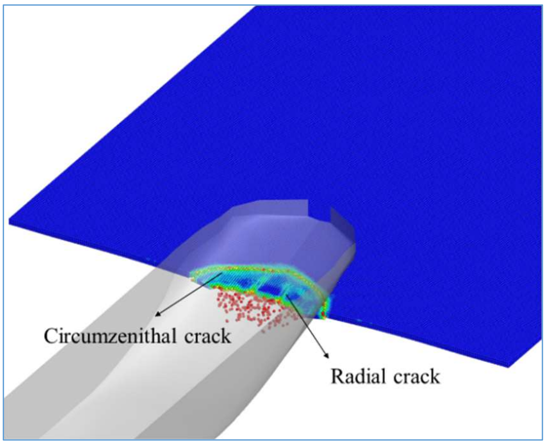

(a)
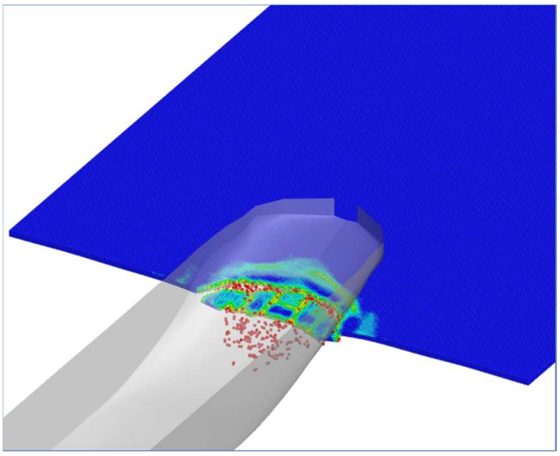
(b)
</td>
</tr>
</table>

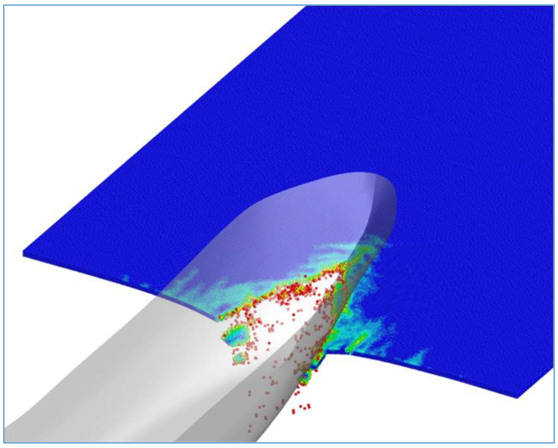

(c)

Fig. 21. Crack propagation of the conventional bow breaking ice

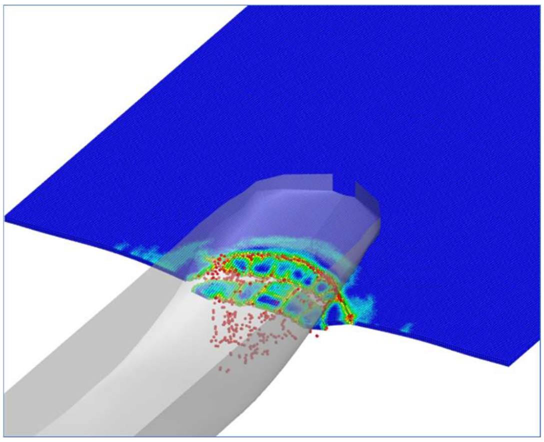

(c)

Fig. 22. Crack propagation of the unconventional bow breaking ice

6.4. Comparison of icebreaking cycle

According to the icebreaking process studied in Section 6.3, it is concluded that the icebreaking process of two kinds of bows follows a certain cycle pattern as time goes by, which is depicted in Fig. 23 and Fig. 24, respectively. It is noted that cracks at different stages are shown in the figure at the same time to demonstrate the evolution of the icebreaking cycle around the bow. As for conventional bow breaking ice, a step in the new cycle starts with the step in the previous cycle at the same time. For example, as shown in Fig. 23, the second circumferential crack at time 1 of Cycle 2 starts to propagate before the large-scale broken ice pieces are entirely bent from the ice sheet at time 2 of Cycle 1. Therefore, there are no explicit behaviors to make a distinction between the two cycles. On the contrary, the unconventional bow icebreaking cycle can be clearly distinguished, and each cycle takes turns. A new cycle begins at the end of the bending failure caused by sufficient propagation of radial cracks of the previous cycle, as shown in Fig. 24.

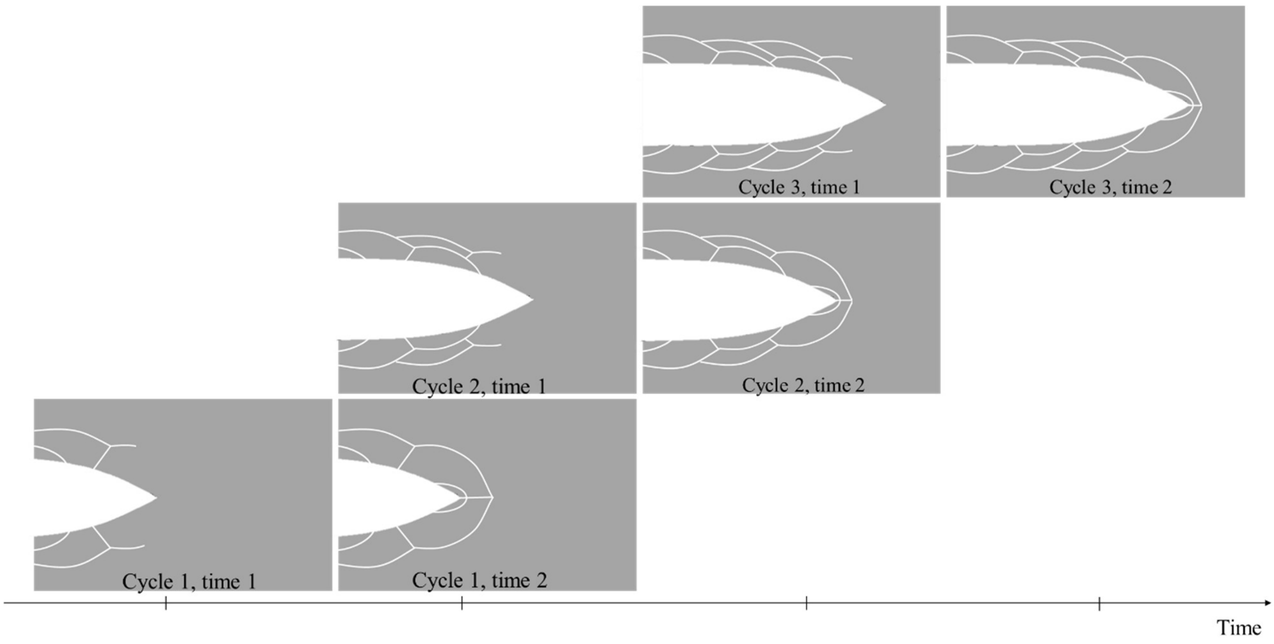

Fig. 23. Icebreaking cycle sketch of the conventional bow breaking ice

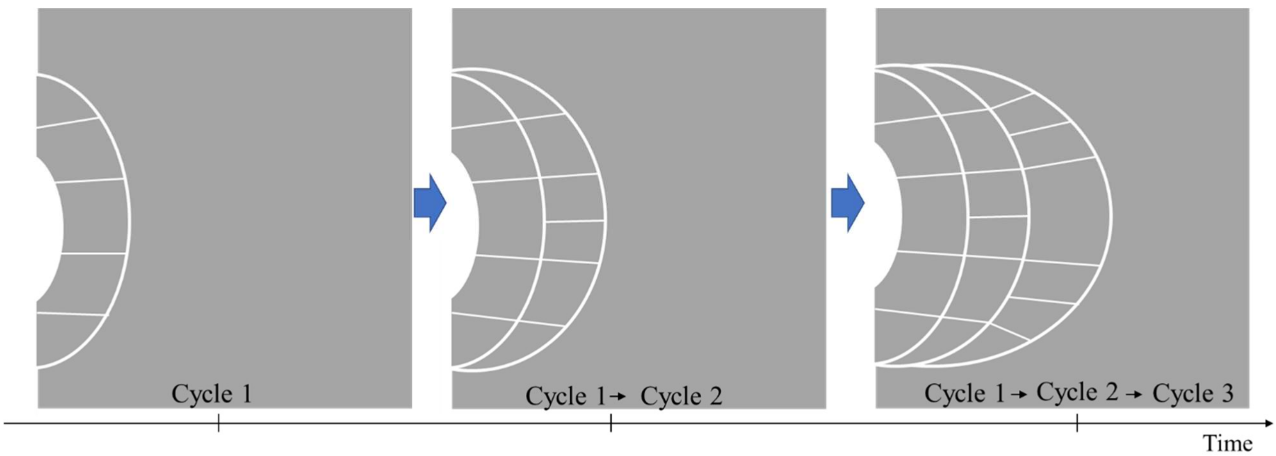

Fig. 24. Icebreaking cycle sketch of the unconventional bow breaking ice

6.5. Icebreaking loads of two bow shapes

The icebreaking loads in time history and their mean value, and the empirical results of the different bows, are shown in Fig. 25 and Fig. 26. The experimental result for the conventional bow is also included in Fig. 25. The force curves show that the ice load trend of the two kinds of bows corresponds to the icebreaking mode as analysed in Section 6.4. The ice load of the traditional bow has the characteristics of continuity because the crack propagations of the next icebreaking cycle and the current icebreaking cycle process simultaneously; the ice load of the non-traditional bow has a clear periodic cycle characteristic. At each period, the increasing process corresponds to the generation and propagation of the circumferential crack, and the decreasing process corresponds to the propagation of radial cracks; The end of the period corresponds to the process that ice blocks are broken from the ice sheet.

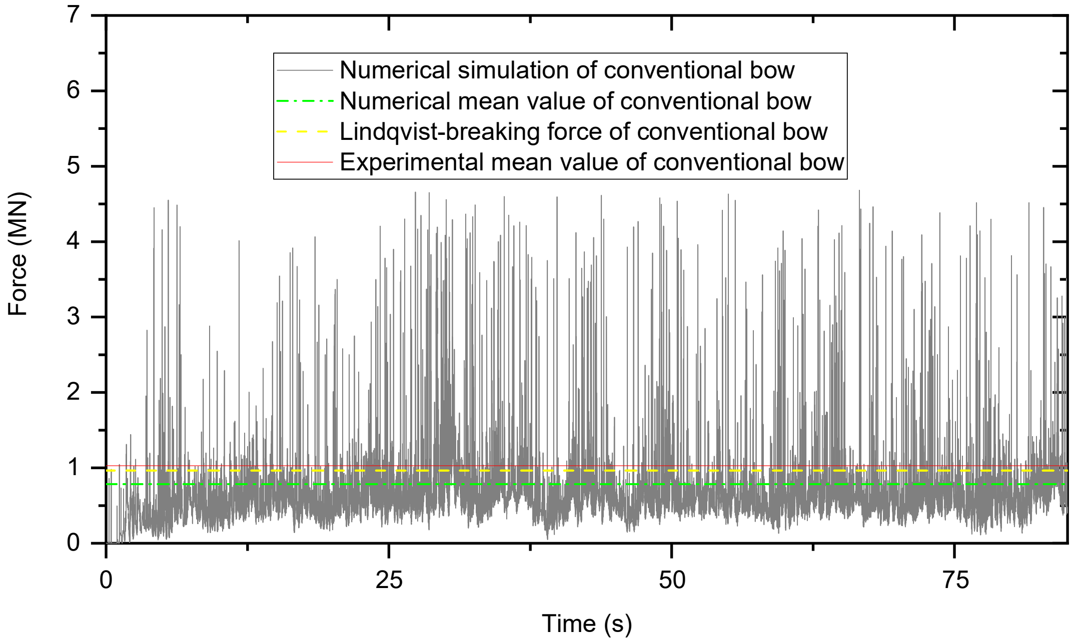

Fig. 25. Icebreaking loads of the conventional bow breaking ice

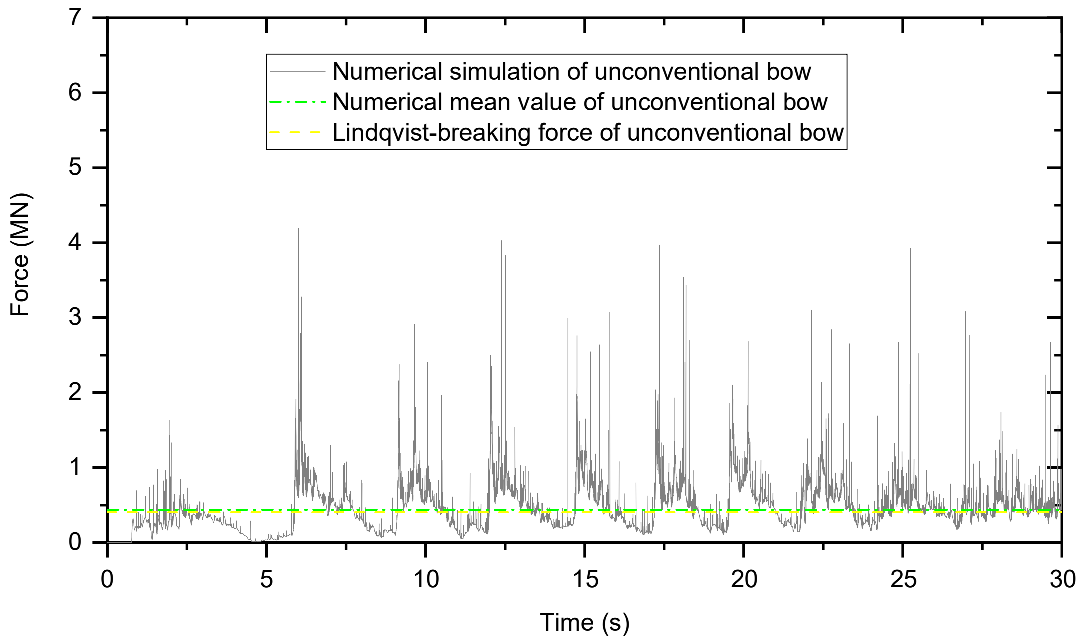

Fig. 26. Icebreaking loads of the unconventional bow breaking ice

6.6. Comparison of the icebreaking channel of the two bows

The width of the traditional extreme bow is 22.6 *m*, and the width of the channel opened is 28.46 *m*. When it comes to the unconventional icebreaker bow, they are 20.0 m and 27.3 m, respectively, as shown in Fig.27 and Fig. 28. The ship breadth could standardise the channel width B, they are W=1.24B and W=1.36B, respectively. Consequently, the ability of the unconventional bow with moderate outline is more remarkable in opening channel.

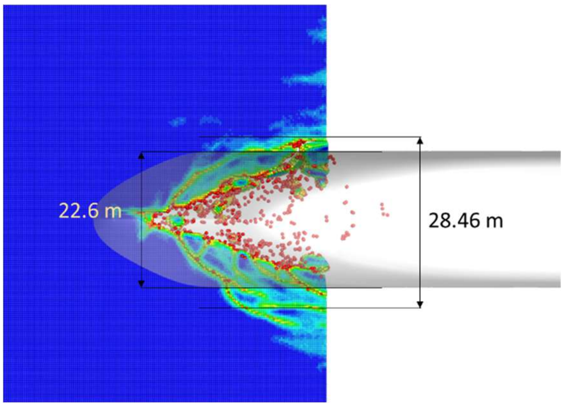

Fig. 27. Icebreaking channel of the conventional bow breaking ice (top view)

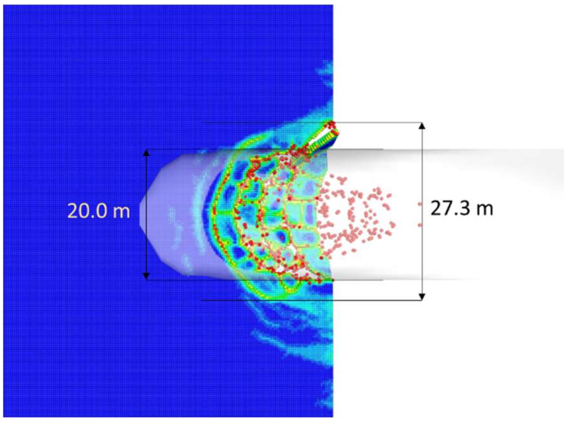

Fig. 28. Icebreaking channel of the unconventional bow breaking ice (top view)

In addition, as shown in Fig. 29 and Fig. 30, it is found that the broken ice pieces of the conventional bow are larger than those broken by the conventional bow, which may further affect the next breaking stage, clearing ice pieces. Finally, the broken ice pieces in the channel opened by conventional bow are mostly pushed onto either side of the bow while the ice pieces are mostly sliding along the gentle bow of the unconventional icebreaker.

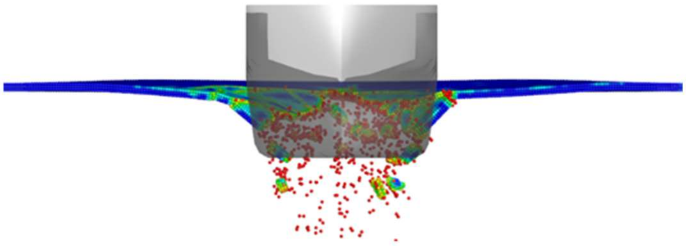

Fig. 29. Icebreaking channel of the conventional bow breaking ice (stern view)

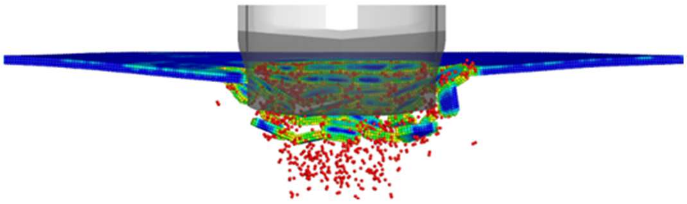

Fig. 30. Icebreaking channel of the unconventional bow breaking ice (stern view)

7. Conclusion

The developed ISI model is effective in the simulation of the icebreaking process, which is proved in Section 6.2. Moreover, it has better accuracy in the prediction of ice damage patterns and cracks propagation than other numerical methods. As a result, the present model successfully investigated the differences between different shape bows, as demonstrated in Section 6.3 and Section 6.4. The following conclusions are obtained:

1) The bow shape has a significant influence on the icebreaking pattern in spite of their common points in domain bending failure mode. The conventional icebreaker with extreme bow shape has multiple forms of crack growth, including radial crack and three circumferential cracks, while the moderate-shaped Thyssen WAAS bow has concise crack propagation pattern with neat circumferential crack and radial crack.
2) There are icebreaking cycles in both bow shapes, but only the cycle of non-traditional bow is clear since its crack growth follows a certain order while crack propagation in the previous cycle and the crack initiation in the next lecture co-occur in the traditional bow icebreaking process.

3) Icebreaking loads also showed a different trend between the two bows. As a result of cyclic icebreaking characteristics, the ice force curve has obvious periodicity for the unconventional bow.
4) Conventional bow broke the ice with a channel width of $W = 1.24B$ while unconventional bow opened a channel with the width of $W = 1.36B$.

8. Limitations of the study and future work

When an icebreaker bow breaks the ice layer, the damaged ice pieces rotate and submerge due to the fluid mechanics. However, the fluid influence on the ice behaviors has not been considered at present work. In future work, the fluid-ice-ship coupled model needs to be developed to investigate the whole icebreaking process.

Acknowledgement

This research was supported by the National Natural Science Foundation of China (Grant No. 51909043), the Natural Science Foundation of Heilongjiang Province of China (Grant NO. E2018026), China Postdoctoral Science Foundation (Grant No. 2020M681082) and China Postdoctoral Science Foundation (Grant NO. 2019M651266).

Reference

Aamot, S.K.G., 2015. A sensitivity study of ice resistance prediction methods using a developed bow shape modelling tool. NTNU.

Cui, X.D., Habashi, W.G., Casseau, V., 2020. MPI Parallelisation of 3D Multiphase Smoothed Particle Hydrodynamics. International Journal of Computational Fluid Dynamics 34 (7-8), 610-621.

Derradji-Aouat, A., 2003. Multi-surface failure criterion for saline ice in the brittle regime. Cold Regions Science and Technology 36 (1-3), 47-70.

Dick, R., Laframboise, J., 1989. An empirical review of the design and performance of icebreakers. Marine Technology and SNAME News 26 (2).

Freitas, A., Nishizaki, R.S., 1986. Model test of an ice class bulk carrier with the Thyssen/Waas bow form. Journal of Energy Resources Technology 108 (2), 168-172.

Gao, T., Erokhin, V., 2020. China-Russia collaboration in arctic shipping and maritime engineering. The Polar Journal 10 (2), 353-374.

Gao, Y., Hu, Z., Ringsberg, J.W., Wang, J.J.O.E., 2015. An elastic–plastic ice material model for ship-iceberg collision simulations. 102, 27-39.

Gao, Y., Oterkus, S., 2019. Ordinary state-based peridynamic modelling for fully coupled thermoelastic problems. Continuum Mechanics and Thermodynamics 31 (4), 907-937.

Glen, I.F., Jones, S.J., Paterson, R.B., Hardiman, K.C., Newbury, S., 1998. Comparative testing of four bow designs for an icebreaking Navaids vessel. Marine Technology and SNAME News 35 (4), 200.

Guard, C.C., 1972. Ice navigation in Canadian waters. Information Canada.

Hu, J., Zhou, L., 2015. Experimental and numerical study on ice resistance for icebreaking vessels. International Journal of Naval Architecture and Ocean Engineering 7 (3), 626-639.

Huang, Y., Huang, S.Y., Sun, J.Q., 2018. Experiments on navigating resistance of an icebreaker in snow covered level ice. Cold Regions Science and Technology 152, 1-14.

Huang, Y., Sun, J.Q., Ji, S.P., Tian, Y.K., 2016. Experimental Study on the Resistance of a Transport Ship Navigating in Level Ice. Journal of Marine Science and Application 15 (2), 105-111.

Ierusalimsky, A., Tsoy, L., 1994. The efficiency of using non-traditional hull lines for icebreakers.

Ishikawa, S., Kawasaki, S., 1995. A Series of Model Tests in Ice of Ice-Going Cargo Ships for Future Traffic in the Northern Sea Route. Ship & Ocean Foundation, 469-474.

ITTC, 2017. Resistance test in ice The International Towing Tank Conference.

Izumiyama, K., Uto, S., 1995. Ice resistance of three bow forms for the nsr cargo ship. Ship & Ocean Foundation, 458-

467.

Jones, S., 2008. A history of icebreaking ships. Journal of Ocean Technology 3 (1), 54-74.

Jones, S.J., 2004. Ships in ice-a review, 25th Symposium on Naval Hydrodynamics.

Jordaan, I.J., 2001. Mechanics of ice-structure interaction. Engineering fracture mechanics 68 (17-18), 1923-1960.

Kishi, S., Narita, S., 1995. Development of Optimum Hull Forms for Icebreaking Cargo Ships for the Northern Sea Route. Ship & Ocean Foundation, 475-482.

Larsen, L.H., Kvamstad-Lervold, B., Sagerup, K., Gribkovskaia, V., Bambulyak, A., Rautio, R., Berg, T.E., 2016. Technological and environmental challenges of Arctic shipping-a case study of a fictional voyage in the Arctic. Polar Research 35 (1).

Lindqvist, G., 1989. A STRAIGHTFORWARD METHOD FOR CALCULATION OF ICE RESISTANCE OF SHIPS, POAC 89, 10th Intl Conference, Port and Ocean Engineering under Arctic Conditions, Luleaa, Sweden.

Lindstrom, C., 1990. Numerical estimation of ice forces acting on inclined structures and ships in level ice, Offshore Technology Conference. Offshore Technology Conference.

Liu, R.W., Xue, Y.Z., Lu, X.K., Cheng, W.X., 2018. Simulation of ship navigation in ice rubble based on peridynamics. Ocean Engineering 148, 286-298.

Lubbad, R., Løset, S., 2011. A numerical model for real-time simulation of ship-ice interaction. Cold Regions Science and Technology 65 (2), 111-127.

Madenci, E., Oterkus, E., 2014. Peridynamic Theory and Its Applications.

Madenci, E., Oterkus, S., 2016. Ordinary state-based peridynamics for plastic deformation according to von Mises yield criteria with isotropic hardening. Journal of the Mechanics and Physics of Solids 86, 192-219.

Michailidis, M., Murdey, D., 1981. Performance of CCGS FRANKLIN in Lake Melville, 1980, Proceeding of the SNAME STAR Symposium, pp. 311-322.

Molyneux, D., 2017. Model Ice: A Review of its Capacity and Identification of Knowledge Gaps, ASME 2017 36th International Conference on Ocean, Offshore and Arctic Engineering. American Society of Mechanical Engineers.

Myland, D., Ehlers, S., 2016. Influence of bow design on ice breaking resistance. Ocean Engineering 119, 217-232.

Noble, P., Bulat, V., 1981. Icebreaker Bow Forms-A Parametric Variation.

Oterkus, S., Madenci, E., Agwai, A., 2014. Peridynamic thermal diffusion. Journal of Computational Physics 265, 71-96.

Palmer, A., Dempsey, J., 2009. Model tests in ice, Proceedings of the International Conference on Port and Ocean Engineering Under Arctic Conditions.

Park, H.-G., Jung, H.-C., Lee, Y.-C., Ahn, S.-M., Hwangbo, S.-M., 2007. A Study on Hull Form Development for Ice Breaking Vessel in the Arctic, Proceedings of the International Conference on Port and Ocean Engineering Under Arctic Conditions.

Prakash, N., Stewart, R.J., 2020. A Multi-threaded Method to Assemble a Sparse Stiffness Matrix for Quasi-static Solutions of Linearized Bond-Based Peridynamics. Journal of Peridynamics and Nonlocal Modeling, 1-35.

Puntigliano, F., 1995. On the Resistance Components Below the Waterline in the Continuous Mode of Icebreaking: Model Tests. Hamburgische Schiffbau-Versuchsanst.

Puntigliano, I.F., 2003. Experimental and Numerical Research on the Interaction between Ice Floes and Ship Hulls during Icebreaking. 2003 97, 269.

Riska, K., 2010. DESIGN OF ICE BREAKING SHIPS.

Riska, K., 2011. Ship–ice interaction in ship design: Theory and practice. Course Material NTNU.

Riska, K., 2019. DESIGN OF ICE BREAKING SHIPS.

Sawamura, J., 2012. Numerical investigation of ice bending failure and ice submerging force for ship maneuvering in level ice, Proc 21st International Symposium on Ice, Dalian, IAHR.

Schulson, E.M., 1990. The brittle compressive fracture of ice. Acta Metallurgica et Materialia 38 (10), 1963-1976.

Schulson, E.M., 1999. The structure and mechanical behavior of ice. JOM 51 (2), 21-27.

Schulson, E.M., 2001. Brittle failure of ice. Engineering fracture mechanics 68 (17-18), 1839-1887.

Schwarz, J., Jochmann, P., Hoffman, L., 1981. Prediction of the icebreaking performance of the German polar research vessel, Proceedings of the 6th STAR Symposium, Ottawa, Canada, pp. 239-248.

Skripnuk, D., Iliyushchenko, I., Kulik, S., Stepanova, M., 2020. Analysis of the current state of the Northern Sea Route and the potential development of the icebreaker fleet, IOP Conference Series: Earth and Environmental Science. IOP Publishing, p. 012129.

Sodhi, D.S., 1995. Northern Sea Route Reconnaissance Study: A Summary of Icebreaking Technology. DIANE Publishing.

Su, B., Riska, K., Moan, T., 2010. A numerical method for the prediction of ship performance in level ice. Cold Regions Science and Technology 60 (3), 177-188.

Suzuki, Y., Uemura, O., Kato, H., Yamaguchi, H., Izumiyama, K., 1997. A Study on Effect of Bow Shape on Icebreaking Resistance. Journal of the Society of Naval Architects of Japan 1997 (181), 75-82.

Tao, F., Chenfang, Y., Yongxu, J., 2019. Estimation of ice resistance and sensitivity analysis for an icebreaker. Advances in Polar Science (4), 7.

Tippmann, J.D., 2011. Development of a strain rate sensitive ice material model for hail ice impact simulation. UC San Diego.

Valanto, P., 2001. On the cause and distribution of resistance forces on ship hulls moving in level ice, Proceedings of the International Conference on Port and Ocean Engineering under Arctic Conditions.

Vazic, B., 2020. Multi-scale modelling of ice-structure interactions. University of Strathclyde.

Vazic, B., Diyaroglu, C., Oterkus, E., Oterkus, S., 2020. Family Member Search Algorithms for Peridynamic Analysis. Journal of Peridynamics and Nonlocal Modeling 2 (1), 59-84.

Vazic, B., Oterkus, E., Oterkus, S., 2019. Peridynamic approach for modelling ice-structure interactions, Trends in the Analysis and Design of Marine Structures: Proceedings of the 7th International Conference on Marine Structures CRC Press, Dubrovnik, Croatia.

Wang, C., Xiong, W.P., Chang, X., Ye, L.Y., Li, X., 2018. Analysis of variable working conditions for propeller-ice interaction. Ocean Engineering 156, 277-293.

Warntjen, J., Erceg, S., Piehl, H., Ehlers, S., 2018. The influence of the bow design on structural response due to ice loading. Ships and Offshore Structures 13 (sup1), 302-311.

White, R., 1969. Prediction of icebreaker capability. Shipping World & Shipbuilder 162 (3838).

Xue, Y.Z., Liu, R.W., Li, Z., Han, D.F., 2020. A review for numerical simulation methods of ship-ice interaction. Ocean Engineering 215.

Yamaguchi, H., Suzuki, Y., Uemura, O., Kato, H., Izumiyama, K., 1997. Influence of bow shape on icebreaking resistance in low speed range, Proceedings of the International Conference on Offshore Mechanics and Arctic Engineering. AMERICAN SOCIETY OF MECHANICAL ENGINEERS, pp. 51-62.

Ye, L.Y., Guo, C.Y., Wang, C., Wang, C.H., Chang, X., 2020. Peridynamic solution for submarine surfacing through ice. Ships and Offshore Structures 15 (5), 535-549.

Ye, L.Y., Wang, C., Chang, X., Zhang, H.Y., 2017. Propeller-ice contact modeling with peridynamics. Ocean Engineering 139, 54-64.

Zhang, Y., Tao, L., Wang, C., Ye, L.Y., Guo, C.Y., 2021. Numerical study on dynamic icebreaking process of an icebreaker by ordinary state-based Peridynamics and continuous contact detection algorithm. Ocean Engineering (in press).